Biosensors and Bioelectronics 191 (2021) 113409

Contents lists available at ScienceDirect

Biosensors and Bioelectronics

journal homepage: www.elsevier.com/locate/bios

Ultrasensitive near-infrared electrochemiluminescence biosensor derived from Eu-MOF with antenna effect and high efficiency catalysis of specific CoS_2 hollow triple shelled nanoboxes for procalcitonin

Lu Zhao [a,b], Xianzhen Song [a,b], Xiang Ren [a,b], Huan Wang [a,b], Dawei Fan [a,b], Dan Wu [a,b,*], Qin Wei [a,b]

[a] Collaborative Innovation Centre for Green Chemical Manufacturing and Accurate Detection School of Chemistry and Chemical Engineering, University of Jinan, Jinan, 250022, Shandong, China

[b] Key Laboratory of Interfacial Reaction & Sensing Analysis in Universities of Shandong, School of Chemistry and Chemical Engineering, University of Jinan, Jinan, 250022, Shandong, China

ARTICLE INFO

Keywords:
Near-infrared
Electrochemiluminescence
Immunoassay
Antenna effect
Hollow core-shell structure
Procalcitonin

ABSTRACT

In this paper, we report a novel multiple amplification strategy for ultrasensitive near-infrared electrochemiluminescence (ECL) immunoassay in $K_2S_2O_8$ solution. The realization of this strategy is based on the antenna effect of Eu-MOF (EuBTC) and a high efficiency catalysis of CoS_2 hollow triple shelled nanoboxes (TSNBs). The H_3BTC ligand in the antenna effect first undergoes π-π^* absorption and a singlet-singlet electronic transition. Its energy passes through the intersystem to the triplet state, next transfers from the lowest excited triplet state to the vibrational energy level of the rare earth ion, finally realizing sensitizing center ion luminescence. Moreover, ionic reaction and structural advantages endow CoS_2 TSNBs a dual signal enhancement effect. This sandwich-type ECL biosensor has a near-infrared luminescence in 800–900 nm, thus avoiding damage to the sample in the meantime. In practical diagnosis, the normal critical value of procalcitonin (PCT) (<0.5 ng/mL) is much higher than the detection limit (3.65 fg/mL) and is in the detection range (10 fg/mL-100 ng/mL), which means that the ECL biosensor has a high sensitivity in the detection of PCT and meet the requirement for diagnosis of disease completely. Therefore, the strategy provides a feasible method for efficient and stable analysis of systemic inflammatory response such as fearful bacterial infection, hepatitis B, and peritonitis.

1. Introduction

Electrochemiluminescence (ECL) immunoassay has possessed massive attention in analytical chemistry with merits of its high sensitivity and stability, low background, wide dynamic ranges, plain operation, benign time and space control over the light emission (Hu and Xu, 2010; Song et al., 2018). On account of ECL is a redox-induced light emission, luminophores that created radicals during own oxidation or reduction process are undoubtedly the most crucial link of whole ECL process (Carrara et al., 2017). Nevertheless, the eminent bottleneck remain in the exorbitant cost between the traditional luminophore such as luminol and $[Ru(bpy)_3]^{2+}$ (Li et al., 2017; Zhang et al., 2017). As a functional luminescent materials, price-friendly luminescent lanthanide complexes (LLCs) have emerged as promising luminophores due to their innate luminescence excellence brought from 4f-4f transitions and ample variety of ladder-like electronic levels, such as supernal luminescent efficiency, long lifetime and intrinsic narrow emission peak (Bünzli and Piguet, 2006; Wei et al., 2016). Surprisingly, LLCs is a kind of material that has be widely used in near-infrared (NIR) luminescence, which is very advantageous for ultrasensitive biological, clinical and drug detection and analysis in harsh environments (heavy pollution, high temperature, high pressure, harmful to human body and equipment), and can avoid damage to the sample and improve the stability of the detection result (Sun et al., 2005; Tymiński et al., 2020; Yu et al., 2021).

Especially, by virtue of its ultrahigh surface area, highly dispersed atomical metal sites and well-defined porosity (Kuang et al., 2018; Zhao et al., 2020), trivalent lanthanide metal-organic frameworks (Ln-MOFs)

* Corresponding author. Collaborative Innovation Centre for Green Chemical Manufacturing and Accurate Detection School of Chemistry and Chemical Engineering, University of Jinan, Jinan, 250022, Shandong, China.
E-mail address: wudan791108@163.com (D. Wu).

https://doi.org/10.1016/j.bios.2021.113409
Received 23 January 2021; Received in revised form 28 May 2021; Accepted 3 June 2021
Available online 11 June 2021

have managed to outsmart other the above LLCs, and become one of them more suitable for ECL luminescence. Highly active catalytic sites make Ln-MOFs has high catalytic activity (Zhao et al., 2019). Moreover, Ln^{3+} coordinate with strong absorbing organic ligands to realize sensitizing center ion luminescence via ligand antenna effect, leading to an enhanced Ln^{3+} luminescence (Li et al., 2018a, 2020a). During the antenna effect, the ligand takes place π-π* absorption at first. Then its energy undergoes an electronic transition from the S_0 singlet state to the S_1 singlet state, and accesses to the triplet state T_0 through the intersystem crossing in the next moment. Next the energy transfers from the lowest excited triplet state T_1 to the vibrational energy level of Ln^{3+}. The ground state of Ln^{3+} is excited and transitioned to the excited state. When the electron returns to the ground state from the excited state energy level, Ln^{3+} emits the characteristic fluorescence (Yang et al., 1994). Thanks to the antenna effect, Ln-MOFs consisted of Ln^{3+} and strong absorbing organic ligands have overcome low quantum yield for luminescence resulted from parity-forbidden f-f transitions and given rise to a colossal enhanced sensitivity to the chemical environments (Li et al., 2020a; Mathieu et al., 2018). These phenomena endow the above Ln-MOFs with strong luminescence and high sensitivity, which makes them better applied in many fields such as immunoassay, detection of various molecules and ions, bioimaging and bioprobes (Charbonniere et al., 2006; Wei et al., 2016).

There is no denying that utilization of coreaction accelerators in sandwich-type biosensor is another feasible strategy to enhance the ECL efficiency of luminophores. For now, ZIF-67 (Song et al., 2020), CeO_2 (Yang et al., 2019) and CuS (Song et al., 2018) as the major materials for catalyzing coreactants to produce reactive intermedium radicals. Especially, since Co^{3+} converted from Co^{2+} during the reaction with $S_2O_8^{2-}$ can be re-converted into Co^{2+}, the nanomaterials containing Co^{2+} can promote the generation of more $SO_4^{\bullet-}$ radicals, thereby enhances the ECL signal. However, the actual desire for high catalytic capacities of nanomaterials constructed with their single structures are far exceeded their abilities. By contrast, complex hollow structure materials can attain the goal of enhancing catalytic activity owing to their high specific surface area and enhanced volume controllability (Chiang et al., 2019). However, utilization of hollow structure materials as coreaction accelerators in ECL fields is still under initial stage, to the best of our knowledge, especially the complex hollow structure materials. Thus, exploring coreaction accelerator's catalytic behavior of complex hollow structure materials will be a subject worthy of research. Herein, we used complex hollow triple shelled nanoboxes (TSNBs) self-assembled only by sole CoS_2 via calcination in Ar as coreaction accelerators, and the CoS_2 TSNBs were transformed from cobalt divanadate TSNBs (Wang et al., 2019). The outstanding combination of transition metal ion and sulfur avoids inevitable weaknesses of insufficient redox sites and poor electrical conductivity in other materials, so that enhances electron transport during catalysis in order to increase the ECL signal exponentially (Tran et al., 2020; Wang et al., 2019).

To sum up, a new-high-efficiency sandwich-type PCT detection biosensor was applied to increase ECL efficiency of EuBTC-$S_2O_8^{2-}$ system dramatically to realize high-efficiency procalcitonin (PCT) detection. PCT is a protein that reflects the activity of the systemic inflammatory response. Its level is elevated in plasma during severe bacterial, fungal, parasitic infections, sepsis, and multiple organ failure. Therefore, the determination of PCT can be used as a parameter to the differential diagnosis of fearful bacterial infection, hepatitis B, peritonitis, and as a monitoring of patients at risk for infection such as surgery and postoperative immunosuppression after organ transplantation period. (Song et al., 2020; Vincenzi et al., 2016). In this work, the EuBTC-Fe_3O_4@Au-Ab_2 was selected as signal probe, which took advantage of the stronger antenna effect between Eu^{3+} and high conjugation structure 1,3,5-Benzenetricarboxylic acid (H_3BTC) (Lucena et al., 2017), so that the coordinated EuBTC has higher luminous efficiency. Eu^{3+} also have higher luminous stability than other lanthanide metal ions. In the meantime, the combination of Fc segments in antibody and HWRGWVC (HVC) improved incubation efficiency of antibody and formed the fixed sites by Au–S bonding, that contributed to establishing efficient and long-lifetime biosensors(Li et al., 2017; Song et al., 2020). In addition, an ion-conversion-exchange strategy was effectually used in controllable building-up process of CoS_2 TSNBs, and the complex hollow structure CoS_2 TSNBs were employed as a catalyst to render $S_2O_8^{2-}$ to create more $SO_4^{\bullet-}$ intermediates and accelerate ECL excitation, and the capture-antibody (Ab_1) was incubated on CoS_2 TSNBs substrate to construct the sensing platform. With a sufficient support of aforesaid strengthening strategies, the self-assembled sandwich-type biosensor exhibited superexcellent ECL performance and sensitivity with detection limit of 3.65 fg/mL.

2. Experimental section

2.1. Chemicals and Apparatus

Procalcitonin (PCT), procalcitonin primary antibody (Ab_1) and secondary antibody (Ab_2) were both brought from Nanjing Kingsrui Technology CO. LTD. HWRGWVC heptapeptide was ordered from GL Biochem. Ltd. (Shanghai, China). DMF, ethanol, $NH_3 \cdot H_2O$, and chloroauric acid tetrahydrate ($HAuCl_4 \cdot 4H_2O$) were all supplied by Sinopharm Chemical. The phosphated buffered solution (PBS) was used as the detection solution which was prepared by mixing KH_2PO_4 (0.1 M) and Na_2HPO_4 (0.1 M). The purity of all reagents which were used in this experiment was analytical grade. All other reagents were acquired from Macklin Industrial Corporation. Furthermore, ultrapure water (18.25 MΩ cm^{-1}) was employed throughout this research.

The morphologies and sizes of as-prepared nanomaterials were characterized by scanning electron microscope (SEM, JEOL JSM-6700F microscope, Japan). X-ray powder diffraction (XRD) patterns were acquired with a D8 advance X-ray diffractometer (Bruker AXS, Germany). Meanwhile, the elemental composition of nanoparticles was obtained by X-ray photoelectron spectroscopy (XPS, Escalab MK II, UK). The UV–vis absorption spectra were acquired by the UV–vis spectrophotometer (UV-2450, Shimadzu, Japan). In addition, the cyclic voltammetry (CV) and electrochemical impedance spectroscopy (EIS) measurements were realized with an electrochemical workstation (Zahner Zennium PP211, Germany). The ECL signals were monitored by the MPI-E Electrochemiluminescence Analyzer (Xi'an remax Electronic Science Tech. Co. Ltd., Xi'an China).

2.2. Preparation of the MOF EuBTC

The materials, regents and apparatus were displayed in the Supporting Information. With hydrothermal synthesis, 0.5 mmol of Eu $(NO_3)_3 \cdot 6H_2O$, and 0.5 mmol of H_3BTC were added in mixture with 20 mL N,N-dimethylformamide (DMF) and 5 mL of ethanol, the solution was transferred into a Teflon-lined stainless steel autoclave and heated at 120 °C in an oven for 24 h. The white crystal was harvested by centrifugation and washed with DMF and ethanol, dried at 60 °C.

2.3. Preparation of CoS_2 TSNBs

The synthesis method of ZIF-67 nanocubes was shown in the Supporting Information, and the entire processes were slightly modified according to the reference (Wang et al., 2019). 45 mg of the synthesized ZIF-67 nanocubes were dispersed into 40 mL ethanol accompanied by ultrasound 5 min, which was named solution A. In the meantime, 0.4 mmol of NH_4VO_3 was dissolved in a mixed solution of 9.5 mL of H_2O and 0.5 mL of $NH_3 \cdot H_2O$ at 60 °C in an oil bath for 3 h. Then the NH_4VO_3 aqueous solution was added into the solution A rapidly with continuous stirring for 1 min. The khaki green products were collected by centrifugation and washed with ethanol for three times and then dried at 60 °C. Whereafter, the products were dispersed in 40 mL of ethanol and heated at 50 °C in an oil bath for 10 min. Then 10 mL of deionized water

was added into it and continued to heat for 4 h. After centrifugation and drying, the resulting powder is continuously dispersed in 45 mL of ethanol, and a mixture of 200 mg of TAA and 5 mL of ethanol was poured into it under constant stirring. The solution was heated at 90 °C in an oil bath for 4 h and centrifugated with ethanol and dried. Finally, the blank products were annealed at 350 °C in Ar for 2 h to obtain the CoS_2 TSNBs.

2.4. Preparation of the EuBTC-Fe_3O_4@Au-Ab_2

Firstly, 100 μL solution mixed by 40 mM 1-(3-(dimethylamino)propyl)-3-ethylcarbodiimide hydrochloride (EDC) and 10 mM sulfo-N-hydroxysulfosuccinimide (NHS) was added into 5 mL sonicated EuBTC solution (4 mg/mL), which was stirred at 4 °C for 2 h. Then 2–3 mL of Fe_3O_4@Au solution (1%) was joined in it to gain EuBTC-Fe_3O_4@Au. After centrifugation, the produces dispersed in 2 mL PBS (pH=7.4) and 200 μL HVC (50 μg/mL), at the same time, stirred for 3 h at 4 °C. Next, add 100 μL of Ab_2 solution (10 μg/mL) and keep incubated for 8 h. 80 μL of BSA was joined in it in the end. After stirring at 4 °C for 2 h, we successfully prepared Ab_2 bioconjugates EuBTC-Fe_3O_4@Au-Ab_2.

2.5. Fabrication process of biosensor

The pithy sensing interface of intramolecular ECL emission was demonstrated in Scheme S1. The bare electrode (GCE) was brightened with polishing powders so that achieved a smooth mirror surface level at the beginning. Secondly, a thin film of Au was electro-deposited on the electrode surface by using $HAuCl_4$ (1%) solution. Then the as-prepared CoS_2 TSNBs and HVC (50 ng/mL) solutions were coated on substrate successively. After dying, the Ab_1 solution (100 μg/mL) was modified onto Au-CoS_2-HVC. Then dropping BSA on above modified electrode to expose the active site. In the following step, electrodes orderly dropped with 10 μL solution of diverse quantities of PCT and fixed concentration of EuBTC-Fe_3O_4@Au-Ab_2 were incubated under the same conditions, which meant successful construction of the biosensor. After each modification step, the electrode needs to be placed for 1.5 h to fully bind the materials to the front layer. Finally, the electrodes were gently washed with ultrapure water to eliminate the nonspecific binding during the fabrication of the immunosensor.

2.6. ECL detection of PCT

The ECL behavior was monitored over the scanning range of −1.8–0 V in 15 mL PBS (pH=8.0) containing 80 mM $K_2S_2O_8$, at a photomultiplier tube voltage of 800 V and a scanning rate of 100 mV/s. The concentrations of EuBTC, $Eu(NO_3)_3 \cdot 6H_2O$ and H_3BTC were all 2.47 × 10^{-6} mol/mL.

3. Result and discussion

3.1. Characterizations of EuBTC-Fe_3O_4@Au bioconjugates

Fig. 1A shows X-ray powder diffraction (XRD) patterns of the as-synthesized EuBTC. Multiple distinct and primary diffraction peaks at 10.08°, 13.14°, 17.18° and 24.54° perfectly match with the (110), (11-1), (130) planes for theoretical XRD simulation of EuBTC (CCDC-290771). Next, FTIR measurement is employed to further analyze the structure of EuBTC. As displayed in Fig. 1B, The disappearance of the distinct band and broad band respectively corresponded to the $V_{C=O}$ at 1700 cm^{-1} and $V_{O\text{-}H}$ at 3300–2500 cm^{-1} that originally existed in the spectrum of H_3BTC as well as meanwhile the appearance of two sets of symmetric peaks at 1612-1555 cm^{-1} and 1442-1383 cm^{-1} severally ascribed to asymmetric and symmetric stretching vibrations of COO^- attests the successful coordination of Eu^{3+} and H_3BTC. The narrow absorption bands range from 650 to 900 cm^{-1} ($\delta_{=C-H}$) imply the presence of aromatic rings (Cai et al., 2019; Haquin et al., 2009). Further, the X-ray photoelectron spectroscopy (XPS) survey spectrum confirms the chemical composition and valence states for EuBTC (Fig. S1A). As seen in the spectra of Fig. 1C, the two protruding binding energies at 1131.1 and 1163.3 eV correspond to Eu $3d_{5/2}$ and Eu $3d_{3/2}$, respectively. Fig. S1B displays the high-resolution O 1s spectrum, the typical peak at 531.9 eV is attributed to O^{2-} (Cai et al., 2019; Chaudhary et al., 2019). All of the above-mentioned results explicitly support the successful preparation of EuBTC.

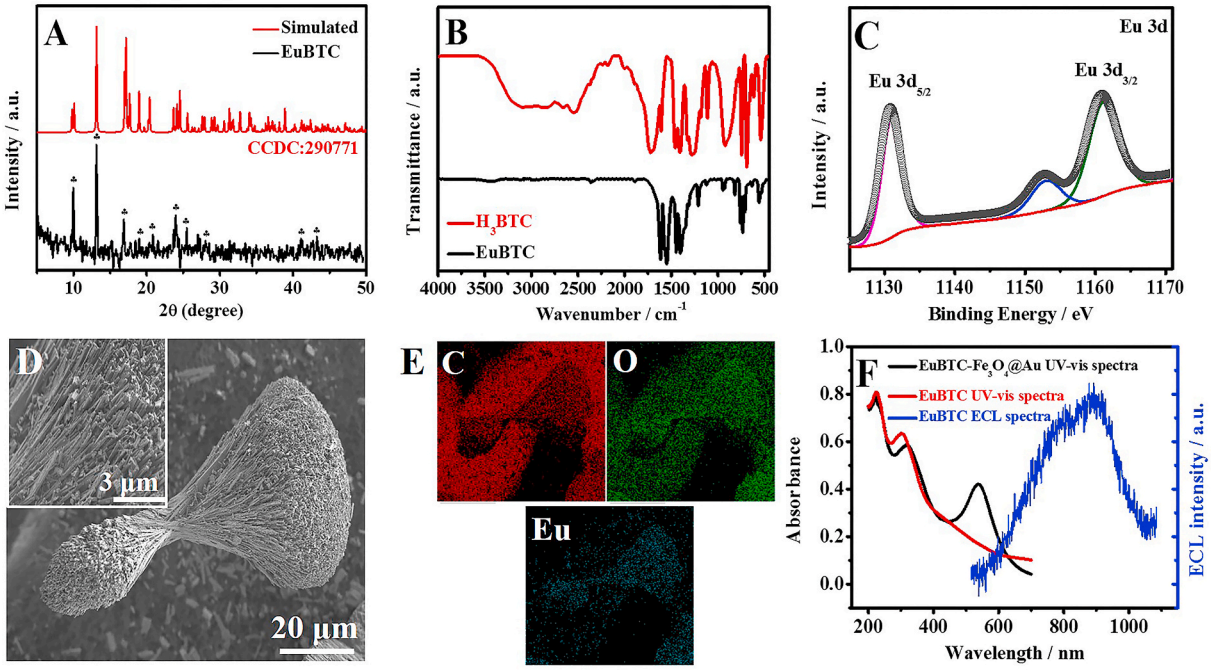

Fig. 1. (A) XRD pattern of as-synthesized and simulated EuBTC. (B) FT-IR spectra of H_3BTC and EuBTC. (C) XPS spectra in the Eu 3d regions for EuBTC. (D) Low- and high magnification SEM images of EuBTC (E) EDX elemental mapping images of Eu, C and O for EuBTC. (F) UV–vis spectra of EuBTC and EuBTC-Fe_3O_4@Au, and ECL spectra of EuBTC.

Even more, the scanning electron microscopy (SEM) exhibits the morphology of as-synthesized EuBTC in Fig. 1D and S2. A broccoli-like appearance constructed of numerous nanorods about 500 nm in width can be seen, and densely arrayed of nanorods result in luxuriant active sites, which contributes to sufficient contact between MOF and electrolyte thereby enhance electronic transmission efficiency and then ECL efficiency. And elemental mappings from energy-dispersive X-ray spectroscopy (EDS) explain an equal distribution of the elements Eu, C and O in the as-prepared EuBTC (Fig. 1E). As for EuBTC-Fe_3O_4@Au, dense nanorods are attributed to coordination of $-NH_2$ and Eu^{3+} during synthesis, and the synthesized Fe_3O_4@Au nanospheres about 200 nm in diameter are evenly and tightly distributed in EuBTC (Fig. S3), which increase the active sites.

In terms of the UV–vis spectra (Fig. 1F), two obvious absorption peaks at 225 nm and 302 nm respectively are both ascribed to H_3BTC π-π* absorption (red curve) (Peng et al., 2018), explicit peak corresponded to Fe_3O_4@Au is reflected at 537 nm (blank curve) (Cai et al., 2012). The characteristic peak of EuBTC is slightly red-shifted when the compound is EuBTC-Fe_3O_4@Au bioconjugates, which indicates the enhancement of conjugation and the successful crosslinking between EuBTC and Fe_3O_4@Au. Additionally, the ECL characteristic peak of EuBTC was fallen on the short wavelength near-infrared (NIR) region 800–900 nm (Fig. 1F), in which the toxicity to biological analytes is less than that of materials with other luminescent wavelengths, as a NIR fluorescent probe, this showed the tremendous potential of EuBTC for biological analysis (De Bonis-O'Donnell et al., 2019).

3.2. Characterizations of CoS_2 TSNBs

Fig. 2A shows the XRD patterns for the as-synthesized CoS_2 TSNBs and simulated diagram. Diffraction peaks at 27.8°, 32.3°, 36.2°, 39.8°, 46.3° and 54.9° can be indexed to the (111), (200), (210), (211), (220) and (311) planes of CoS_2 phase, respectively (JCPDS No. 41–1471). Fig. S5 shows the XPS survey of CoS_2 TSNBs, further confirming the presence of Co and S elements. The Co 2p spectrum shown in Fig. 2B can be divided into four peaks which are assigned to $2p_{3/2}$ of Co^{2+} (782.8 eV) and $2p_{1/2}$ of Co^{2+} (798.0 eV), as well as the corresponding satellite peaks (identified as "Sat.") at 784.0 and 805.5 eV arise from Co^{2+}. In addition, the S 2p (Fig. 2C) peaks at 162.9 and 164.1 eV are assigned to S $2p_{3/2}$ and S $2p_{1/2}$ in CoS_2 severally (Cui et al., 2019; Zhang et al., 2018). SEM images reveal that the CoS_2 TSNBs samples have a cubic morphology about 300 nm in length and further transmission electron microscope (TEM) images reveal that the hollow triple shelled nanoboxes are faultlessly formed in sulfidation process and withstood under calcination at 350 °C (Fig. 2D–F) after the form of cobalt divanadate TSNBs resulted from divanadate ion seriatim underwent ion exchange reaction with the inner core ZIF-67 twice. And through energy-dispersive X-ray spectroscope (EDX) analysis and SEM elemental mapping we are clear at a glance for uniform distribution of Co and S element in CoS_2 TSNBs samples (Fig. S6).

3.3. Testification of enhancement of electro-active surface area and electron transfer of CoS_2 TSNBs

The excellent changes in structure are undoubtedly beneficial for the improvement of material performance, like the change of TSNB of CoS_2 in this work, which improves electrochemically active surface area and electron transfer rate of catalysis compared with CoS_2 with ordinary structure, thus improves ECL signal. To prove it, we calculate electroactive surface area of CoS_2 and CoS_2 TSNBs measured with cyclic voltammetry (CV) on the basis of Randles-Sovcik equation (Yang et al., 2019):

$$I = 2.69\times10^5\, AD^{1/2}n^{3/2}v^{1/2}c$$

and the CV was tested under $K_3[Fe(CN)_6]$ environment.

In this equation, I means the peak reduction current of $K_3[Fe(CN)_6]$, A means the electrochemical active area (cm^2) to be calculated, D is the diffusion coefficient of $[Fe(CN)_6]^{4-/3-}$ at room temperature, which is 6.70×10^{-6} cm^2 s^{-1} approximately. n and v mean the number of electron transfer and scanning rate during this test respectively, c means the concentration of $K_3[Fe(CN)_6]$ solution.

Based on the slopes of reduction peak values vs scan rates in these CVs (Fig. 3A–B) (The linear fitting equations are $I = 389.94\, v^{1/2} + 65.7$ and $I = 974.12\, v^{1/2} + 11.6$, respectively), the obtained A value of CoS_2

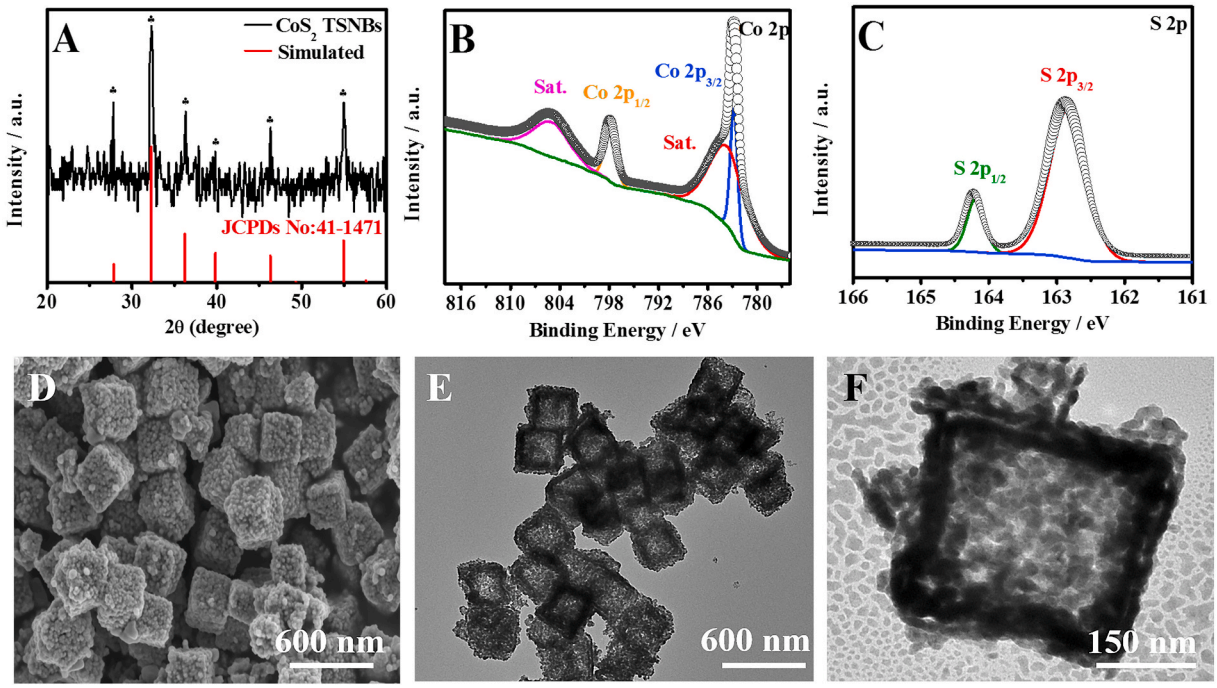

Fig. 2. (A) XRD pattern of as-synthesized and simulated CoS_2. XPS spectra in the (B) Co 2p and (C) S 2p regions for CoS_2 TSNBs. (D) SEM and (E–F) TEM images of CoS_2 TSNBs.

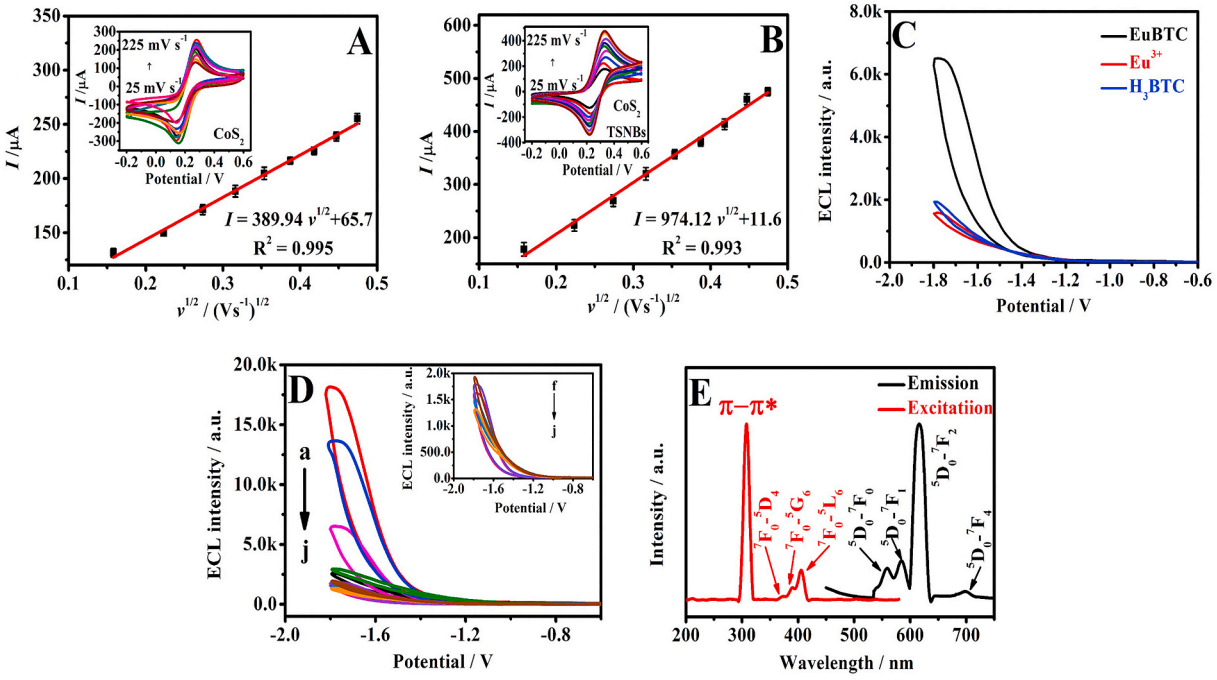

Fig. 3. CV curves and linear relations of electrodes modified with (A) CoS_2 and (B) CoS_2 TSNBs in 5.0 mmol/L of $[Fe(CN)_6]^{4-/3-}$ in scan rates range of 25–225 mV s^{-1}. Error bars = SD, (n = 3). (C) ECL-potential curves of various luminophors of EuBTC, H_3BTC and Eu^{3+}. (D) ECL-potential curves of diverse conditions: EuBTC-CoS_2 TSNBs, EuBTC-CoS_2 and EuBTC systems in $S_2O_8^{2-}$ solution, EuBTC, EuBTC-CoS_2 TSNBs and EuBTC-CoS_2 systems in PBS, H_3BTC and Eu^{3+} in $S_2O_8^{2-}$ solution, H_3BTC and Eu^{3+} in PBS, which follow the curves a-j sequence. The inset figure was the enlarged curves of f-j sequence. (E) Excitation and emission spectra of EuBTC. (All concentrations of tested materials were 2.47 × 10^{-6} mol/mL).

TSNBs is 28.00 mm^2, bigger than 11.20 mm^2 of CoS_2, displaying the significant increase of electro-active surface area for CoS_2 TSNBs due to synthesis of complex triple shelled hollow structure. In addition, it's worth noting that the improvement of electron transfer rate is illustrated via the increase of current responses of CoS_2 TSNBs compared with CoS_2.

3.4. Speculation of ECL enhanced mechanism

The effect of complex hollow structure for catalytic ability is proved by above calculation of electro-active surface area and analysis of electron transfer rate improvement, which on the strength of ECL signal

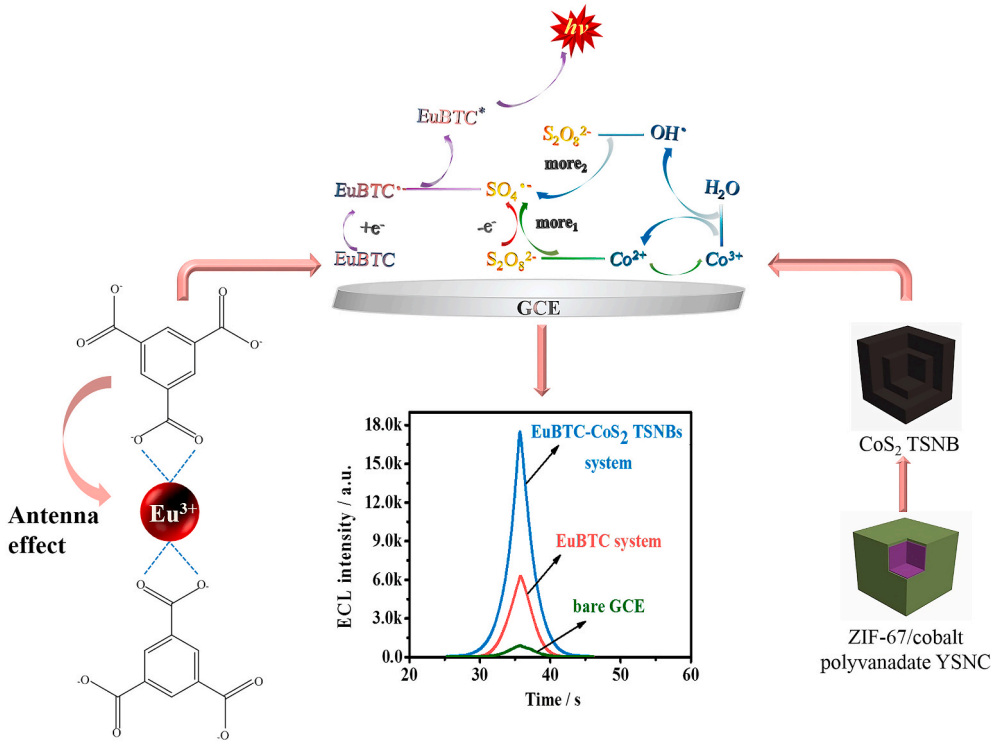

Scheme 1. The mechanism illustration of the increased ECL by antenna effect and dual enhancement effect of CoS2 TSNBs.

is shown in the Fig. 3D, from which distinct comparison of bare EuBTC, EuBTC-CoS_2 system and EuBTC-CoS_2 TSNBs system with ECL intensity of 6278.50, 13640.55, and 17501.94 au are displayed, severally. The specific enhancement strategy of CoS_2 as coreaction accelerator is speculated as follows (Song et al., 2020): with the assistance of CoS_2, $S_2O_8^{2-}$ decomposes more $SO_4^{\bullet-}$, and oxidizes Co^{2+} to Co^{3+} concurrently (equation (2)), then the neonatal Co^{3+} are supposed to be converted to Co^{2+} in the reverse process, which together with the generation of $OH^{\bullet}$, results in the production of $SO_4^{\bullet-}$ once again through the reaction between $OH^{\bullet}$ and $S_2O_8^{2-}$ (equations (3)–(6)). Last but not least, a large number of $SO_4^{\bullet-}$ react with $EuBTC^{\bullet-}$ in the hole of EuBTC to generate more plentiful EuBTC*, thereby enhances the ECL efficiency. The whole conjectural mechanism is shown as follows in the form of equations and Scheme 1:

Path 1:

$$S_2O_8^{2-} + e^- \rightarrow SO_4^{2-} + SO_4^{\bullet-} \quad (1)$$

Path 2:

$$Co^{2+} + S_2O_8^{2-} \rightarrow Co^{3+} + SO_4^{2-} + SO_4^{\bullet-} \text{ (more)} \quad (2)$$

Path 3:

$$4Co^{3+} + 2H_2O \rightarrow 4Co^{2+} + 4H^+ + O_2 \quad (3)$$

$$O_2 + H_2O + e^- \rightarrow H_2O_2 + OH^- \quad (4)$$

$$H_2O_2 + e^- \rightarrow OH^- + OH^{\bullet} \quad (5)$$

$$OH^{\bullet} + S_2O_8^{2-} \rightarrow O_2 + HSO_4^- + SO_4^{\bullet-} \text{ (more)} \quad (6)$$

ECL emission:

$$EuBTC + e^- \rightarrow EuBTC^{\bullet-} \quad (7)$$

$$EuBTC^{\bullet-} + SO_4^{\bullet-} \rightarrow EuBTC^* + SO_4^{2-} \quad (8)$$

$$EuBTC^* \rightarrow EuBTC + h\nu \quad (9)$$

This dual enhancement strategy of CoS_2 TSNBs, which consists of large specific surface area and wonderful catalytic activity of complex hollow triple shelled structure and special reaction mechanism of Co^{2+}, results in greater enhancement ability for ECL signal than other coreaction accelerators.

In addition, we compared ECL signals of bare EuBTC system and EuBTC-CoS_2 TSNBs system in respective $K_2S_2O_8$ and PBS coreactant, trying to verify whether CoS_2 only catalyzes the coreactant. As can be seen in Fig. 3D, curves d and e show the ECL intensity of bare EuBTC system and EuBTC-CoS_2 TSNBs system in PBS respectively, low and indiscriminate values of both indicate sole effect of CoS_2 for $K_2S_2O_8$ rather than act on EuBTC.

Ascensive luminous efficiency of EuBTC resulted from the antenna effect is compared with bare Eu^{3+} and H_3BTC ligand (Fig. 3C). Low and indiscriminate values of bare Eu^{3+} and H_3BTC ligand are surpassed trebly and much by EuBTC. This is because the antenna effect that generated by following Jablonski energy transfer principle, that is the organic ligand, which is played a role of antenna, fully absorbs optical energy, then transfers the energy to the central rare earth ion coordinated with it through the molecular energy transfer mode, the detailed process is as described in the preface. To ulteriorly attest the antenna effect, we performed optical performance test included absolute quantum yield (QY), excitation and emission spectra test of EuBTC. The QY of EuBTC was detected at room temperature and exhibited an average QY of approximately 20%. From Fig. 3E, an excitation maxima is ascribed to energy transfer from the $\pi-\pi^*$ of the H_3BTC to the emissive center, peaking at 308 nm with less intensity peaks at 350–420 nm matched with Eu^{3+} excitation bands triggered by f-f transitions of Eu^{3+}. The emission spectrum expresses $^5D_0-^7F_J$ (J = 0,1,2,4) transitions of Eu^{3+} with optimal emission wavelength at 616 nm. Among them, $^5D_0-^7F_1$ and $^5D_0-^7F_2$ are magnetic dipole and electric dipole transition, severally. The f→f transition of bare Eu^{3+} is originally a "parity forbidden", but other parity components are mixed after the form of EuBTC, and the symmetry of EuBTC is reduced, which generates "Induced electric dipole transition", thus results in the significant enhancement of luminescence efficiency. In addition, the EuBTC can produce better fluorescence effect than Eu^{3+} indicated that the lowest triplet energy level of H_3BTC can be better matched with the excited state energy level of Eu^{3+}. Above phenomena illustrated that the antenna effect, which realized L*→M (Intramolecular non-radiative energy transfer occurs from the excited state ligand to the metal ion, and then transitions to the ground state of the metal ion to emit light), is the most leading excitation mechanism for EuBTC (Lucena et al., 2017; Wehner et al., 2016; Zhou et al., 2013).

3.5. Electrochemical performance of the biosensor

Ordinal assembly process of the sensor is characterized through CV intuitively. As shown in Fig. S8A, the biosensor with various modification states were tested in an electrolyte containing 2.5 mM $[Fe(CN)_6]^{3-}$ and 0.1 M KCl. Compared with bare GCE, a rising peak tendency of GCE/DpAu demonstrates that the electron shift speed is accelerated. The subsequent dripping of CoS_2 TSNBs hinders the electron transport brought from AuNPs, which cause decline of current peak, but it is still higher than bare GCE. However, as HVC, Ab_1, BSA, PCT and EuBTC-Fe_3O_4@Au-Ab_2 with poor electrical conductivity were modified on the electrode surface, a downdrift of current peak shows up. The above results reveal the successful constructing of proposed biosensor.

Electrochemical impedance spectroscopy (EIS), except CV, is a supplementary mean for judging successful preparation of biosensor by stepwise-modified electrode. From Fig. S8B, the impedance has a smallest semicircle when GCE is only filled with AuNPs, which results from the outstanding conductivity of AuNPs. But after dipping CoS_2 TSNBs on GCE/DpAu, the resistance increased due to the barrier of electron transfer of CoS_2 TSNBs. Whereafter, with the sequential coverage of HVC, Ab_1, BSA, PCT and EuBTC-Fe_3O_4@Au-Ab_2, the resistance increased one by one, and the variation trend of EIS is in accord with that result of CV, proves the successful constructing of proposed biosensor.

3.6. ECL analysis of as-fabricated immunosensor

Sensitive quantitative analysis for PCT are conducted through using the proposed biosensor with the aid of optimized environment, and explicit as well as regular variation trend is observed in corresponding ECL intensity-time curve (Fig. 4A). In the meantime, more digitized, visualized and exact demonstration is utilized via calibration curve (logarithm of PCT concentration and ECL intensity are abscissa and ordinate respectively), which was expressed by with $I = 1936.59 \lg c + 183.37$ whose correlation coefficient was 0.992 (Fig. 4B). Compared with those in previous papers, the as-fabricated immunosensor has a lower detection limit calculated at 3.65 fg/mL. The good sensitivity of this proposed biosensor endows it with superiority for efficient detection of PCT that in order to outsmart other methods and biosensors (Table 1).

3.7. The demonstration of the as-fabricated immunosensor for stability, repeatability and selectivity

In addition to good sensitivity, a preeminent biosensor's evaluation criteria must also have outstanding participation of stability, repeatability and selectivity. In terms of stability for PCT detection, a satisfactory result was attested via a low RSD of 1.7% calculated on the basis of 9 cycles of continuous electrodes scanning, as shown in Fig. S9. However, it is not enough to maintain outstanding stability only in a short term, and it can be put into practical application after a long period of storage with benign stability. From Fig. 4C, after 20 days of storage at 4 °C, compared with the ECL signal without HVC, lower falling range of

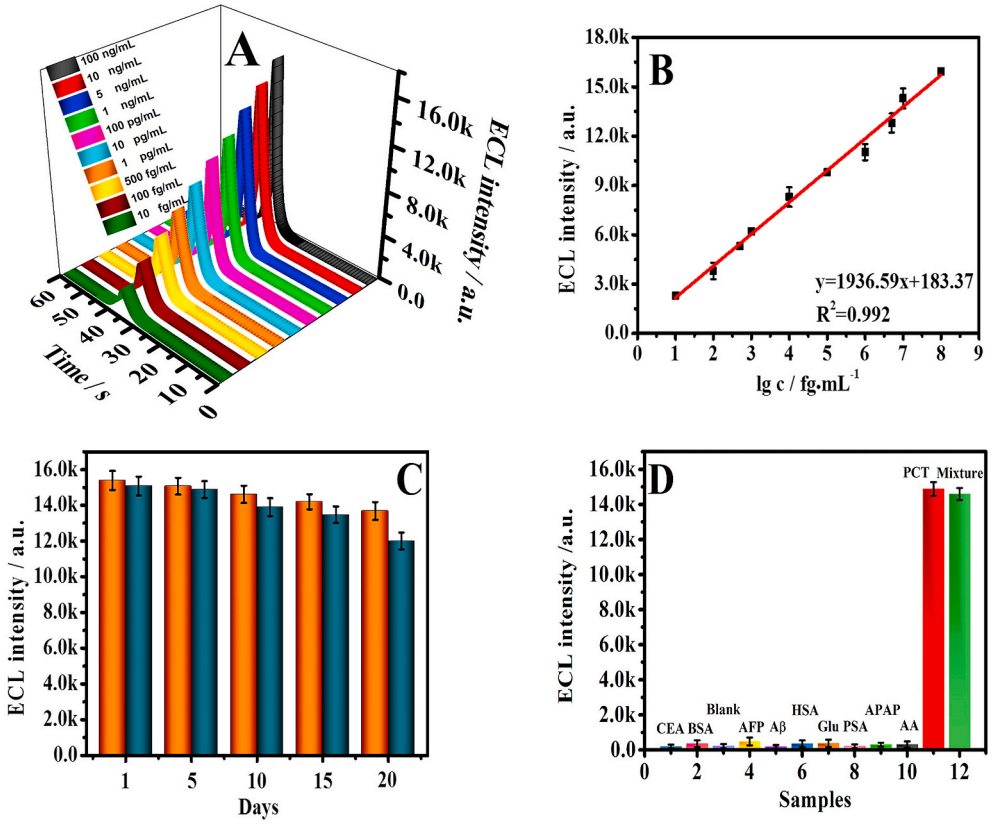

Fig. 4. (A) Corresponding ECL intensity-time curve and (B) Calibration curve of the constructed immunosensor for procalcitonin detection with a wide concentration range (10 fg/mL to 100 ng/mL) (C) ECL intensity stability of the proposed biosensor with and without HVC under different days conservation. (D) Specificity tests of biosensors for 10 ng/mL PCT and mix with 100 ng/mL diversified interferent: carcinoembryonic antigen (CEA), bovine serum albumin (BSA), alpha-fetoprotein (AFP), amyloid-β (Aβ), human serum albumin (HSA), glucose (Glu), prostate-specific antigen (PSA), acetaminophen (APAP) and ascorbic acid (AA). Error bars = SD, (n = 3).

Table 1
Comparison of different proposed biosensors for PCT detection.

Methods	Linear range (ng/mL)	Detection limit (pg/mL)	References
ECL	0.00001–100	0.00365	This work
Imaging ellipsometry	0.13–128	81.0	Li et al. (2018b)
Microfluidic	0.005–4	3.0	Liang et al. (2012)
Electrochemical	0.01–20	1.74	Liu et al. (2014)
ECL	0–75	<1000	Zhou and Xia (2018)
ECL	0.0001–50	0.0826	Li et al. (2020b)
ECL	14–40	0.0034	Fang et al. (2021)
ECL	0.00001–100	0.00367	Song et al. (2020)

ECL signal for the proposed biosensor contained HVC illustrates the assistance of introduction of HVC for biosensor's stability. In addition, blurry difference of the ECL signal owned a low RSD of 0.74% indicated an excellent repeatability of the as-fabricated immunosensor (Fig. S10).

If benign stability and reproducibility can target any detection object, then it will be a meaningless sensor. A specific biosensor, as the name implies, only detects and analyzes a specific substance. Therefore, we test ECL signals with different interferences included carcinoembryonic antigen, bovine serum albumin, alpha-fetoprotein, amyloid-β, human serum albumin, glucose, prostate-specific antigen, acetaminophen and ascorbic acid. As shown in Fig. 4D, the interference signal is nearly alike the blank signal, while the mixed detection signal (10 ng/mL of PCT +100 ng/mL of interferences) is almost the same as the PCT detection signal, which demonstrates the well selectivity as a specific biosensor for PCT.

3.8. Analysis of real samples

The human serum samples obtained from local hospital were measured 5 times and the relative standard deviation (RSD) was calculated to acquire the precision. Before the test, serum samples were pretreated by centrifugation three times and the supernatant was taken as initial sample. As can be seen from Fig. 4D and S12, the matrix effect in serum is very small, which has little influence on the detection results. As shown in Table S1, the recovery rate is calculated with a range from 98.0 to 103% intensively with low RSD between 1.3 and 2.4%, verifying a wonderful accuracy of the proposed biosensor in real samples and fitting for practical applications of PCT clinical diagnosis.

4. Conclusions

In conclusion, we have built a near-infrared novel and high-efficiency sandwich-type PCT detection biosensor with EuBTC and CoS_2 TSNBs as luminophore and coreaction accelerators due to the antenna effect of EuBTC and dual enhancement effect of CoS_2 TSNBs. And the combination of Fc segments in antibody and HVC improved incubation efficiency of antibody and formed the fixed sites by Au–S bonding, that contributed to establishing efficient and long-lifetime biosensors. Compared to traditional luminophores such as luminol and $[Ru(bpy)_3]^{2+}$ and noble metal catalysts, the Eu-MOF and CoS_2 make the ECL biosensor possess a lowcost advantage. The ECL biosensor owns a wide detection range (10 fg/mL-100 ng/mL) and a low detection limit (3.65 fg/mL). The normal critical value (<0.5 ng/mL) of PCT is much higher than the detection limit and is in the detection range, and the detection limit is lower than most of previously reported ECL biosensors, which means that the ECL biosensor has a high sensitivity in the detection of PCT. Simultaneously the biosensor owns wide detection range, good stability, reproducibility and practicability, which makes it meet the requirement for diagnosis of disease completely. And its characteristic of near-infrared can realize no damage sample test and

adapt harsh environment. Moreover, this biosensor has a high selectivity to PCT, which can better avoid the interference of other substrates in serum. Therefore, the construction of the biosensor is a feasible idea for efficient and ultrasensitive PCT detection.

CRediT authorship contribution statement

Lu Zhao: Conceptualization, Data curation, Writing – original draft. **Xianzhen Song:** Methodology, Data curation, Writing – review & editing. **Xiang Ren:** Methodology. **Huan Wang:** Formal analysis. **Dawei Fan:** Methodology, Supervision. **Dan Wu:** Funding acquisition, Project administration, Writing – review & editing. **Qin Wei:** Funding acquisition, Formal analysis.

Declaration of competing interest

The authors declare that they have no known competing financial interests or personal relationships that could have appeared to influence the work reported in this paper.

Acknowledgment

This work was supported by the Young Taishan Scholars Program of Shandong Province (tsqn201909124), the National Natural Science Foundation of China (21775054), the Project of "20 items of University" of Jinan (2019GXRC018) and the National Key Scientific Instrument and Equipment Development Project of China (21627809). All of authors express their sincere thanks.

Appendix A. Supplementary data

Supplementary data to this article can be found online at https://doi.org/10.1016/j.bios.2021.113409.

References

Bünzli, J.C.G., Piguet, C., 2006. Chem. Soc. Rev. 34, 1048–1077.
Cai, Y.J., Li, X.Y., Wu, K.B., Yang, X.F., 2019. Anal. Chim. Acta 1062, 78–86.
Cai, H.D., Li, K.A., Shen, M.W., Wen, S.H., Luo, Y., Peng, C., Zhang, G.X., Shi, X.Y., 2012. J. Mater. Chem. 22, 15110–15120.
Carrara, S., Arcudi, F., Prato, M., De Cola, L., 2017. Angew. Chem. Int. Ed. 56, 4891-4891.
Charbonniere, L., Hildebrandt, N., Ziessel, R.F., Loehmannsroeben, H.G., 2006. J. Am. Chem. Soc. 128, 12800–12809.
Chaudhary, S., Kumar, S., Mehta, S.K., 2019. Mater. Sci. Eng. C 96, 263–271.
Chiang, C.Y., Huang, T.T., Wang, C.H., Huang, C.J., Tsai, T.H., Yu, S.N., Chen, Y.T., Hong, S.W., Hsu, C.W., Chang, T.C., Chau, L.K., 2019. Biosens. Bioelectron. 151, 111871.
Cui, Y., Chen, F., Yin, X.B., 2019. Biosens. Bioelectron. 135, 208–215.
De Bonis-O'Donnell, J.T., Pinals, R.L., Jeong, S., Thakrar, A., Wolfinger, R.D., Landry, M. P., 2019. Biochemistry 58, 54–64.
Fang, J.L., Li, J.S., Feng, R.Q., Yang, L., Zhao, L., Zhang, N., Zhao, G.H., Yue, Q., Wei, Q., Cao, W., 2021. Sens. Actuators, B 332, 129544.
Haquin, V., Gumy, F., Daiguebonne, C., Bünzli, J.C., Guillou, O., 2009. Eur. J. Inorg. Chem. 29–30, 4491–4497.
Hu, L.Z., Xu, G.B., 2010. Chem. Soc. Rev. 39, 3275–3304.
Kuang, X., Luo, Y.C., Kuang, R., Wang, Z.L., Sun, X., Zhang, Y., Wei, Q., 2018. Carbon 137, 433–441.
Li, Y., Liu, W., Jin, G., Niu, Y., Chen, Y., Xie, M., 2018b. Anal. Chem. 90, 8002–8010.
Li, Y.Y., Liu, L., Liu, X.J., Ren, X., Xu, K., Zhang, N., Sun, X.J., Yang, X.L., Ren, X., Wei, Q., 2020b. Biosens. Bioelectron. 163, 112280.
Li, X.J., Lu, S., Tu, D.T., Zheng, W., Chen, X.Y., 2020a. Nanoscale 12, 15021–15035.
Li, Y., Jiang, Z.W., Xiao, S.Y., Huang, C.Z., Li, Y.F., 2018a. Anal. Chem. 90, 12191–12197.
Li, Z.Y., Lin, Z.F., Wu, X.Y., Chen, H.T., Chai, Y.Q., Yuan, R., 2017. Anal. Chem. 89, 6029–6035.
Liang, W., Li, Y., Zhang, B., Zhang, Z., Chen, A., Qi, D., Yi, W., Hu, C., 2012. Biosens. Bioelectron. 31, 480–485.
Liu, F., Xiang, G.M., Chen, X.M., Luo, F.K., Jiang, D.N., Huang, S.G., Li, Y., Pu, X.Y., 2014. RSC Adv. 4, 13934–13940.
Lucena, M.A.M., Oliveira, M.F.L., Arouca, A.M., 2017. ACS Appl. Mater. Interfaces 9, 4684–4691.
Mathieu, E., Sipos, A., Demeyere, E., Phipps, D., Sakaveli, D., Borbas, K.E., 2018. Chem. Commun. 54, 10021–10035.
Peng, J.F., Guo, Y., Xu, X.Y., Tang, Z.H., 2018. J. Lumin. 208, 479–487.
Song, X.Z., Li, X.J., Wei, D., Feng, R., Yan, T., Wang, Y.G., Ren, X., Du, B., Ma, H.M., Wei, Q., 2018. Biosens. Bioelectron. 126, 222–229.
Song, X.Z., Shao, X.R., Dai, L., Fan, D.W., Ren, X., Sun, X., Luo, C.N., Wei, Q., 2020. ACS Appl. Mater. Interfaces 12, 9098–9106.
Sun, L.N., Zhang, H.J., Meng, Q.G., Liu, F.Y., Fu, L.S., Peng, C.Y., Yu, J.B., Zheng, G.L., Wang, S.B., 2005. J. Phys. Chem. B 109, 6174–6182.
Tran, D.T., Hoa, V.H., Le, H.T., Kim, N.H., Lee, J.H., 2020. J. Mater. Chem. A. 8, 14746–14756.
Tymiński, A., Śmiechowicz, E., Martín, I.R., Grzyb, T., 2020. ACS Appl. Nano Mater. 3, 6541–6551.
Vincenzi, B., Fioroni, I., Pantano, F., Angeletti, S., Dicuonzo, G., Zoccoli, A., Santini, D., Tonini, G., 2016. Sci. Rep. 6, 28090–28095.
Wang, X., Chen, Y., Fang, Y.J., Zhang, J.T., Gao, S.Y., Lou, X.W., 2019. Angew. Chem. Int. Ed. 25, 2675–2679.
Wehner, T., Mandel, K., Schneider, M., Sextl, G., Mueller-Buschbaum, K., 2016. ACS Appl. Mater. Interfaces 8, 5445–5452.
Wei, H.B., Zhao, Z.F., Wei, C., Yu, G., Liu, Z.W., Zhang, B., Bian, J., Bian, Z.Q., Huang, C. H., 2016. Adv. Funct. Mater. 26, 2085–2096.
Yang, L., Jia, Y., Wu, D., Zhang, Y., Ju, H.X., Ma, H.M., Wei, Q., 2019. Anal. Chem. 91, 14066–14073.
Yang, Y.S., Gong, M.L., Li, Y.Y., Lei, H.Y., Wu, S.L., 1994. J. Alloys Compd. 207–208, 112–114.
Yu, H.H., Liu, Q., Li, J., Su, Z.M., Li, X., Wang, X.L., Sun, J., Zhou, C., Hu, X.L., 2021. J. Mater. Chem. C. 9, 562–568.
Zhang, J.Y., Liu, Y.C., Sun, C.Q., Xi, P.X., Peng, S.L., Gao, D.Q., Xue, D.S., 2018. ACS Energy Lett 3, 779–786.
Zhang, X., Guo, W.W., Wang, Z.M., Ke, H., Zhao, W.J., Zhang, A.M., Huang, C.S., Jia, N. Q., 2017. Sens. Actuators, B 253, 470–477.
Zhao, L., Kuang, X., Kuang, R., Tong, L., Liu, Z.X., Hou, Y., Sun, X., Wang, Z.L., Wei, Q., 2020. ACS Appl. Mater. Interfaces 12, 1533–1538.
Zhao, L., Kuang, X., Sun, X., Zhang, Y., Wei, Q., 2019. J. Electrochem. Soc. 166, H534–H540.
Zhou, J.M., Shi, W., Li, H.M., Li, H., Cheng, P., 2013. J. Phys. Chem. C 118, 416–426.
Zhou, M., Xia, Y., 2018. Anal. Chim. Acta 1023, 29–34.